Journal of the Civil Engineering Forum, May 2022, 8(2):157-168
DOI 10.22146/jcef.3842
Available Online at https://jurnal.ugm.ac.id/jcef/issue/archive

Finite Element Analysis of Bi-directional Shear Panel Damper with Square Hollow Section under Monotonic Loading

Ali Awaludin[1], Angga Fajar Setiawan[1,*], Imam Satyarno[1], Wu Shuanglan[2], Yusuf Haroki[2]
[1]Department of Civil and Environmental Engineering, Universitas Gadjah Mada, Yogyakarta, INDONESIAA
Jalan Grafika No 2 Yogyakarta
[2]Earthquake Disaster Prevention Engineering Department, Port and Airport Research Institute, JAPAN
Yokosuka, Kanagawa
*Corresponding author: angga.fajar.s@ugm.ac.id

SUBMITTED 12 October 2021 **REVISED** 29 December 2021 **ACCEPTED** 13 January 2022

ABSTRACT This study aims to determine the finite element analysis of a BSPD-SHS (bi-directional shear panel damper with a square hollow section) device, to dissipate the seismic excitation energy through the lateral relative displacement between the pier and girder of the simple support bridge. The configuration of the square hollow section is also performed for a double role, such as web panel and flange, indicating the expectations to reduce the seismic force within the lateral and longitudinal directions. In the preliminary development phase, the finite element analysis was conducted under monotonic loading, to examine the skeleton curve characteristics and internal stress action on resisting seismic force. The characteristics of this curve include elastic stiffness, shear strength, post-yield behavior, and internal stress distributions. Based on the evaluation of the BSPD-SHS slenderness effect, the variation of depth-thickness ratio was considered between 25 to 67. To investigate the fitness of the theoretical shear strength formulation, two different hardening roles of the metal plasticity model were subsequently compared in this study, including the elastic-perfectly plastic and isotropic/kinematic techniques. Furthermore, the effect of the restrained degree of freedom idealization on the top base plate was captured. This indicated that all specimens model with the restrained top base plate achieved stable post-yield stiffness. In implementing the unrestrained top base plate, this stiffness was achieved when the web slenderness ratio equaled 25. The differences observed between the hardening roles also generated a slight yield shear strength discrepancy. However, significant differences occurred in the post-yield shear strength. The shear resistance proportion of the stress components was also accurately quantified with an analytical stress integration. Based on the restrained top base plate, the flange tension field generated a significant contribution to the post-yield shear resistance.

KEYWORDS BSPD-SHS; Web Slenderness; Skeleton Curve, Restrained Top Base Plate, Internal Stress

1 INTRODUCTION

Many kinds of metallic shearing dampers have reportedly been developed for the additional dissipation energy device of structural systems in the last five decades (Abebe et al., 2019; Nuzzo et al., 2018; Maleki and Bagheri, 2010) . Based on the application for bridge structures, these dampers had a role as the stopper or shear key of the upper design relative to the substructure (Tetsuhiko et al., 2010; Tetsuhiko, 2011; Yasuhisa et al., 2007). Also, it is found to contribute to the dissipation of earthquake excitation energy. In Vasseghi (2011), the implementation of metallic yielding-damper reduced the seismic demand of the substructure, due to being the shear key for bridge superstructure. One of the shearing dampers often used is the SPD (shear panel damper), which reportedly has early yielding occurrence. The present application of this damper type is based on the structural strength and energy dissipation enhancement of the integrated multiple-column bridge pier, according to Ge et al. (2012), Sun et al. (2004), NAKAMURA et al. (2014), as well as Chen et al. (2007). Another scheme of the SPD implementation focuses on the simple support bridges, which is conducted through the connection between the superstructure and pier, to achieve energy dissipation. This is due to the relative displacement during an earthquake (Tetsuhiko et al., 2010). The advantages of this damper application are the high energy dissipation achievement, steel component

affordability, simple fabrication, and the economical material, compared to other seismic devices. The common SPD also contains the web, which produces shear resistance with high strain ductility, as illustrated in Fig. 1 (a) and (b). It also contains flanges, which dense the shear stress distribution and prevents the early buckling occurrence of the web in confinement conditions. .

Several studies related to the SPD behaviour and seismic performance have reportedly been conducted by Chen et al. (2007),Chaofeng et al. (2017), Xu et al. (2016), and Hashimoto et al. (2016). Another concept of the SPD development is found through the square hollow section (SHS), as the flange and base plate part for the addition of the web confinement (Chan et al., 2009). Moreover, the common and developed configuration of the SPD devices only accommodates one-directional seismic resistance in a web plane. When an earthquake occurs in the application of seismic devices on the bridge structure, the superstructure is reportedly displaced within longitudinal and transverse directions, simultaneously relative to the pier. This indicated that the developed SPDs by Chan et al. (2009) and Tetsuhiko, Yuuji, and Tatsumasa (2010) were not accommodated in both longitudinal and transverse directions on the bridge structure seismic load. However, the complicated configuration of common SPD should be installed in the longitudinal and lateral directions, as shown in Fig. 1 (c) and (d). This indicated the necessity in developing an SPD device, which is resistant to the seismic load in the longitudinal and lateral directions, with sufficient shear strength and inelastic stability.

Based on the aforementioned descriptions, this preliminary study aims to develop a BSPD-SHS (bi-directional shear panel damper with a square hollow section), which contains a panel and a base plate. The panel parts also contain the welding assembly of four low-yield strength rectangular steel plates with box formation, as illustrated in Fig. 2 (a) and (b). The low-yield strength of these plates is found to contain the LY225 steel (Yamaguchi et al., 1998). Also, the base plate parts contain the ordinary strength (SS400) rectangular steel plate. Under the lateral load (X direction) parallels to the two steel plates in the X-Z plane, both tools performed as the dominant shear force resistant web, as shown in Fig. 2 (c) and (d). This indicates that the two steel plates in the Y-Z plane played the role of the flange. These observations were different from the box-shaped damper (BSD) developed by Shirinkam and Razzaghi (2020), where the energy dissipation was produced by the bending yield mechanism due to the concentrated axial tension-compression load, which was perpendicular to the holding edges of the box section. In this study, the BSPD-SHS focuses on the seismic energy dissipation device on the simple-support structural bridge system. This is based on dissipating the seismic excitation energy through the longitudinal and transverse relative displacement between the pier and girder.

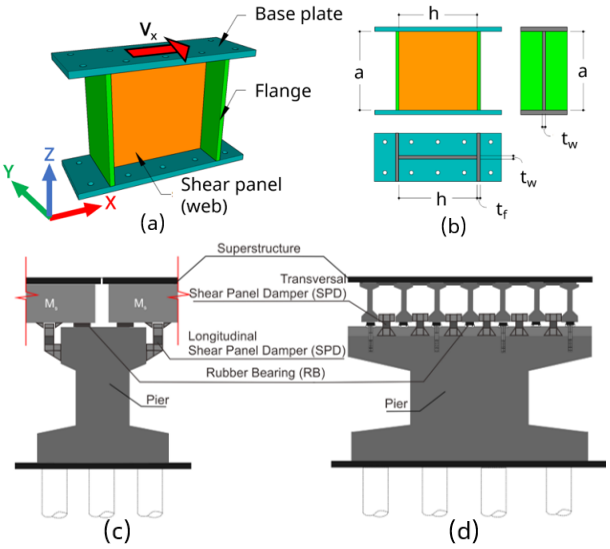

Figure 1 The structural configuration of; (a) common SPD device in 3D view and (b) plan view, (c) the installation of common SPD to the bridge structure in the longitudinal direction, and (d) in the transversal direction

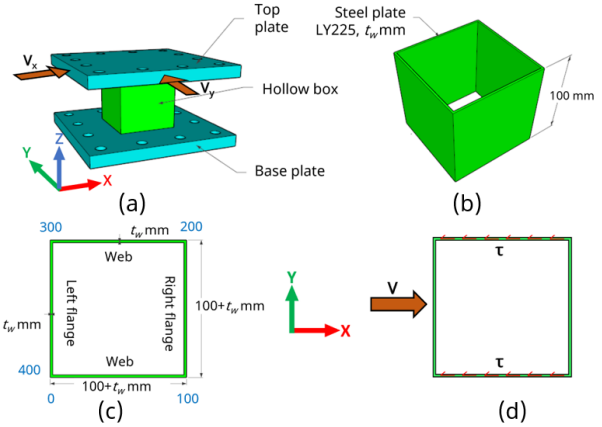

Figure 2 The configuration of BSPD-SHS specimens; (a) the components and the probable lateral load direction, (b) the 3D view of the SHS, (c) the top cutting view of the SHS cross-section, and (d) the load and shear stress reaction schematic.

According to the finite element analysis (FEA) under monotonic loading, the skeleton curve characteristics and internal stress distributions of the proposed device were investigated, where the FEA considered non-linear material and geometry without the reckoning fracture damage of the metal. As an initial study, the BSPD-SHS was subjected to monotonic loading in one direction, parallel to one of the web planes. The most important influential factor on the seismic behavior of this device is the web slenderness, indicating that the skeleton curves characteristics such as elastic stiffness, yield shear strength, and post-yield behavior were examined under four different depth-thickness ratios of the steel plate panel, at 66.67, 50.00, 33.33, and 25.00. In addition, two different hardening roles of the metal plasticity model were presented, to capture the conformity of the numerical design to the analytical approach. The effect of the restrained moment within the rotational degree of freedom idealization was also examined on the top base plate, as the elastic stiffness, shear strength, post-yield behavior, and internal stress action were evaluated to select the best performance of the proposed device, according to the skeleton curve characteristics. Therefore, the shear resistance from the stress components was confirmed with the analytical approach.

2 RESEARCH METHODS

The BSPD-SHS numerical model dimension was scaled at 1:2, with the shear strength less than 150 kN. This was based on fitting with the experimental study plan, where the limit capacity of the load cell was 200 kN. The height and width values of the device were also determined as 100 mm, respectively. In this study, four web slenderness (depth-thickness ratio, λ) variables of the steel plate were subsequently observed, as shown in Table 1. The finite element method was also adopted to solve the non-linear analysis problem (Effendi, 2020).

2.1 Variables of the BSPD-SHS numerical model configuration

The design of the BSPD-SHS shear strength abided with the theoretical stress analysis, where the initial yield occurred in the middle of the web (Hearn, 1997), as expressed in Equations (1), (2), and (3). This strength was denoted as V_y, and proportional to the shear yield stress (τ_y), the moment inertia of section (I), and the web slenderness parameter (C_{v2}), which was 1 when less than the limit criteria as formulated in Equation (2) (AISC, 2016b). Based on other parameters, h, a, w, t, and k_v = the web depth, height, flange width, thickness, and elastic buckling coefficient, respectively. The BSPD-SHS shear resistance behavior was also equal to the square section steel member, where the PSR (principle shear resistance) was dominated by only the two planes of the parallel cross-sectional direction, as shown in Fig. 2 (d). Subsequently, the elastic stiffness of the device contained the ESS and EFS [elastic shear and flexural stiffness](Xu et al., 2020), as formulated in Equations (4-6), where K_s, K_f, and K_c = the ESS, EFS, and blended rigidities (ESS and EFS), respectively. In addition, δ_y, γ_y, and τ_y = the yielding displacement, strain, and stress, while G, E, and v = the shear and elastic moduli, as the Poisson ratio, respectively.

$$V_y = \frac{8\tau_y I}{h^2 + \frac{a+2t_w}{2t_w}\left[(h+2t_w)^2 - h^2\right]} \cdot C_{v2} \tag{1}$$

$$\text{If} \quad \frac{h}{t_w} < 1.10\sqrt{\frac{k_v E}{F_y}}; C_{v2} = 1 \tag{2}$$

$$\text{with} \quad k_v = 5.34 \tag{3}$$

$$K_s = \frac{V_y}{\Delta_y} \quad \text{with} \quad \delta_y = \gamma_y a; \quad \gamma_y = \frac{\tau_y}{G}; \quad \text{and} \quad G = \frac{E}{2(1+\nu)} \tag{4}$$

$$K_f = \frac{12EI}{a^3} \quad \text{and} \quad K_f = \frac{3EI}{a^3}$$

for the restrained and unrestrained top base plates, respectively

(5)

$$K_c = \frac{K_s K_f}{K_s + K_f} \tag{6}$$

Based on this study, the influence of restrained top base plate degree of freedom (DOF) was considered to investigate the post-yield behavior, where the first and second conditions were observed as the R and UR (Restrained and Unrestrained) cases, respectively. This plate restrain was then assigned

in the vertical (UZ), horizontal (UY), and three-rotational (RX, RY, and RZ) degrees of freedom, respectively. The displacement load was also assigned in the lateral direction, which was parallel to the X-axis (UX) in the R and UR treatments of the top base plate. This indicated that the bottom base plate was fixedly idealized in all degrees of freedom. These cases were based on a fundamental point related to the setting option of the seismic device installation in the bridge structural system. When the top base plate was restrained, the device also achieved positive post-yield stiffness, although the occurrence of a large buckling displacement was still observed. This fatigue was due to the repetition of live load, which should be impending the seismic device in long-term failure. Meanwhile, the device was secured from the fatigue phenomenon when the unrestrained DOF of the top base plate was implemented, the device might be secure from the fatigue phenomenon, although post-yield stability was still the main issue. The R and UR of the BSPD-SHS numerical models are shown in Table 1.

2.2 Numerical modelling

Based on the FEA of the BSPD-SHS, the continuum shell element with metal plasticity material model (Dassault-Systèmes, 2011) was adopted for the web panel and base plate parts. This was carried out through the Abaqus software with the consideration of non-linear geometry in all cases of the BSPD-SHS models, to simulate the inelastic buckling occurrence of the panel part. Meanwhile, the geometric imperfection was not considered, due to the elastic buckling limit of all models being designed beyond the shear yield strength. To realize the monolith action between the web and base plates, the tie constraint interaction was adopted, where two steel materials were subsequently proposed and adopted in this study, including the metal plasticity with elastic-perfectly plastic (EPP) and combined isotropic-kinematic hardening (CH). The adoption of these materials followed the procedures of Chaboche (1986), where the variable of the utilized model was shown in Table 2. For the web panel and base plate parts, the metal plasticity and hardening parameters of the LY225 and SS400 steel materials were in line with Shi et al. (2018), Narendra et al. (2019), and Jin et al. (2016), respectively, as shown in Table 2. The elastic-perfectly plastic (EPP) and combined hardening (CH) of the LY225 material constitutive model were also calibrated in the uniaxial tensile analysis, based on Shi et al. (2018). In addition, the linear and non-linear geometries (LG and NLG)

Table 1. Variables of BSPD-SHS numerical model

Name of specimens model	Dimension (mm)				$\lambda = \frac{h}{tw}\sqrt{\frac{Vy}{}}$	(kN)	Top base plate	Mat. model	Name of specimens model	Dimension (mm)				$\lambda = \frac{h}{tw}\sqrt{\frac{Vy}{}}$	(kN)	Top base plate	Mat. model
	h	a	w	tw						h	a	w	tw				
SPD-1.5-R-CH	100	100	100	1.5	66.7	29.58	R	CH	SPD-3.0-R-CH	100	100	100	3.0	33.3	60.16	R	CH
SPD-1.5-R-EPP	100	100	100	1.5	66.7	29.58	R	EPP	SPD-3.0-R-EPP	100	100	100	3.0	33.3	60.16	R	EPP
SPD-1.5-UR-CH	100	100	100	1.5	66.7	29.58	UR	CH	SPD-3.0-UR-CH	100	100	100	3.0	33.3	60.16	UR	CH
SPD-1.5-UR-EPP	100	100	100	1.5	66.7	29.58	UR	EPP	SPD-3.0-UR-EPP	100	100	100	3.0	33.3	60.16	UR	EPP
SPD-2.0-R-CH	100	100	100	2.0	50.0	39.70	R	CH	SPD-4.0-R-CH	100	100	100	4.0	25.0	81.03	R	CH
SPD-2.0-R-EPP	100	100	100	2.0	50.0	39.70	R	EPP	SPD-4.0-R-EPP	100	100	100	4.0	25.0	81.03	R	EPP
SPD-2.0-UR-CH	100	100	100	2.0	50.0	39.70	UR	CH	SPD-4.0-UR-CH	100	100	100	4.0	25.0	81.03	UR	CH
SPD-2.0-UR-EPP	100	100	100	2.0	50.0	39.70	UR	EPP	SPD-4.0-UR-EPP	100	100	100	4.0	25.0	81.03	UR	EPP

Table 2. Mechanical and hardening parameters of steel material idealization

Metallic Material	Elastic Modulus (MPa)	No. of backstress	$\sigma\|0$ (MPa)	Ck,1 (MPa)	$\gamma 1$	Ck,2 (MPa)	$\gamma 2$	Ck,3 (MPa)	$\gamma 3$	Ck,4 (MPa)	$\gamma 4$	Q∞	b
EPP	202,500	-	191	-	-	-	-	-	-	-	-	-	-
CH	202,500	4	191	3,041.0	126.0	1,028	170	890	224	260	1	115	9
SS400	200,000	2	256	1,617.2	10.7	54	0	-	-	-	-	320	20

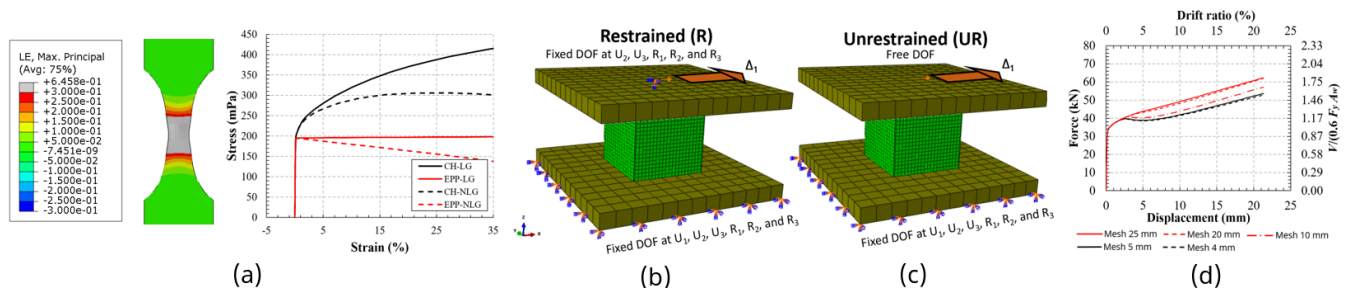

Figure 3 Structural modelling; (a) tensile test calibration of steel material model, (b) top base plate restrained (R), (c) top base plate unrestrained (UR), and (d) mesh convergent study.

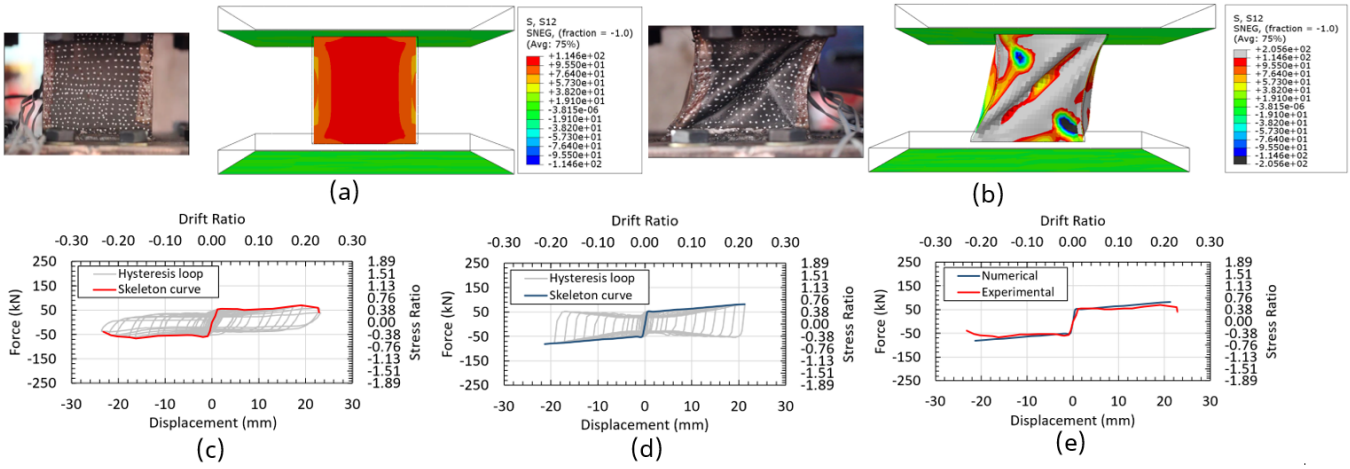

Figure 4 Comparison of the numerical model with the experimental result; (a) deformed shape in yielding state, (b) deformed shape in around 21 mm of deformation, (c) hysteresis loop and skeleton curve of the experimental result, (d) hysteresis loop and skeleton curve of the numerical model result, and (e) comparison of the skeleton curve.

were considered, as shown in Fig. 3 (a).

According to the uniaxial tensile modelling, the EPP material generated a flat and linear softening post-yield stiffness when using the LG and NLG, respectively. Meanwhile, the positive post-yield modulus increased in the idealization of LG and NLG through the combined hardening (CH) material model. Using CH with a linear geometry, a sharper post-yield modulus was generated, compared to the CH with NLG. This indicated that the application of a non-linear geometry generated a softer post-yield modulus, due to the cross-sectional contraction under tension elongation. In this study, the steel material model of the BSPD-SHS did not consider the fracture damage design for the investigation of crack occurrence and propagation, due to high strain or stress concentration. To validate the numerical model, the convergence study and comparative experimental analysis were conducted. According to the convergence study, the implementation of 4 and 5 mm mesh sizes generated a coincidental skeletal curve result through slenderness of 33.3, as shown in Fig. 3 (d). This indicated that the 5 mm mesh size achieved convergence criteria, subsequently leading to the adoption in this study. Based on the comparative experimental result, a good agreement was observed between the skeletal curve and deformed numerical model shape through the slenderness of 58.8, as shown in Fig.4.

Where $\sigma|0$ = yield stress at zero plastic strain, Ck,1 and Ck,2 = kinematic hardening modulus, as well as $\gamma 1$ and $\gamma 2$ = the rates of the kinematic hardening modulus decrease with increasing plastic deformation. The Poisson's ratio (υ) of the LY225 and SS400 materials were also 0.3, as Q∞ = the maximum amplitude of the change in the yield surface size, and b = the rate of change in the yield surface size with the development of plastic strain.

3 RESULT AND DISCUSSION

Based on the FEA, the BSPD-SHS behavior was evaluated, as the elastic stiffness was found to be an important point related to the balancing of the ini-

tial natural period with the bridge structural system. The shear strength performed in controlling the plasticity of this system was also a point of concentration. Furthermore, the post-yield behavior was related to the shear resistance stability in plastic deformation, where the internal stress action of the components was a principal point in capturing the mechanism related to the analytical approach and proportion.

3.1 Elastic Stiffness

According to Table 3 and Fig.4, the restrained specimens model (R) achieved larger elastic stiffness than the unrestrained (UR) type. This was related to the weaker flexural stiffness of the member with the only restrained bottom base plate, compared to those with both tools conditions, including the top and bottom base plates. Moreover, the restrained and unrestrained model stiffness achieved good and soft (21%) agreements with the analytical results, respectively, as shown in Table 3. The yield displacement of the unrestrained numerical models was also larger than the analytical results. This indicated that the restrained and unrestrained models generated the yield displacement values of approximately 0.16 and 0.22% of drift ratio, respectively. However, the hardening material model slightly affected the elastic stiffness.

Table 3. The elastic stiffness and the shear yield stress comparison of the BSPD-SHS

Specimens model	Numerical		Analytical		Relative differences		Specimens model	Numerical		Analytical		Relative differences	
	$K_{c,num}$ kN/mm	$V_{y,num}$ kN	$K_{c,sa}$ kN/mm	$V_{y,sa}$ kN	K_c %	V_y %		$K_{c,num}$ kN/mm	$V_{y,num}$ kN	$K_{c,sa}$ kN/mm	$V_{y,sa}$ kN	K_c %	V_y %
SPD-1.5-R-CH	191.55	29.86	193.03	29.58	0.77	0.95	SPD-3-R-CH	387.19	60.36	393.44	60.16	1.61	0.33
SPD-1.5-R-EPP	191.39	29.84	193.03	29.58	0.86	0.87	SPD-3-R-EPP	386.96	60.32	393.44	60.16	1.67	0.27
SPD-1.5-UR-CH	129.80	28.74	157.21	29.58	21.12	2.92	SPD-3-UR-CH	264.92	58.65	321.95	60.16	21.53	2.57
SPD-1.5-UR-EPP	129.27	28.62	157.21	29.58	21.62	3.35	SPD-3-UR-EPP	264.43	58.54	321.95	60.16	21.75	2.76
SPD-2-R-CH	256.21	39.94	259.28	39.70	1.20	0.59	SPD-4-R-CH	521.08	81.23	530.67	81.03	1.84	0.25
SPD-2-R-EPP	256.02	39.91	259.28	39.70	1.27	0.52	SPD-4-R-EPP	520.84	81.19	530.67	81.03	1.89	0.21
SPD-2-UR-CH	174.22	38.57	211.46	39.70	21.38	2.94	SPD-4-UR-CH	357.83	79.22	435.66	81.03	21.75	2.28
SPD-2-UR-EPP	173.64	38.44	211.46	39.70	21.78	3.28	SPD-4-UR-EPP	357.40	79.12	435.66	81.03	21.90	2.40

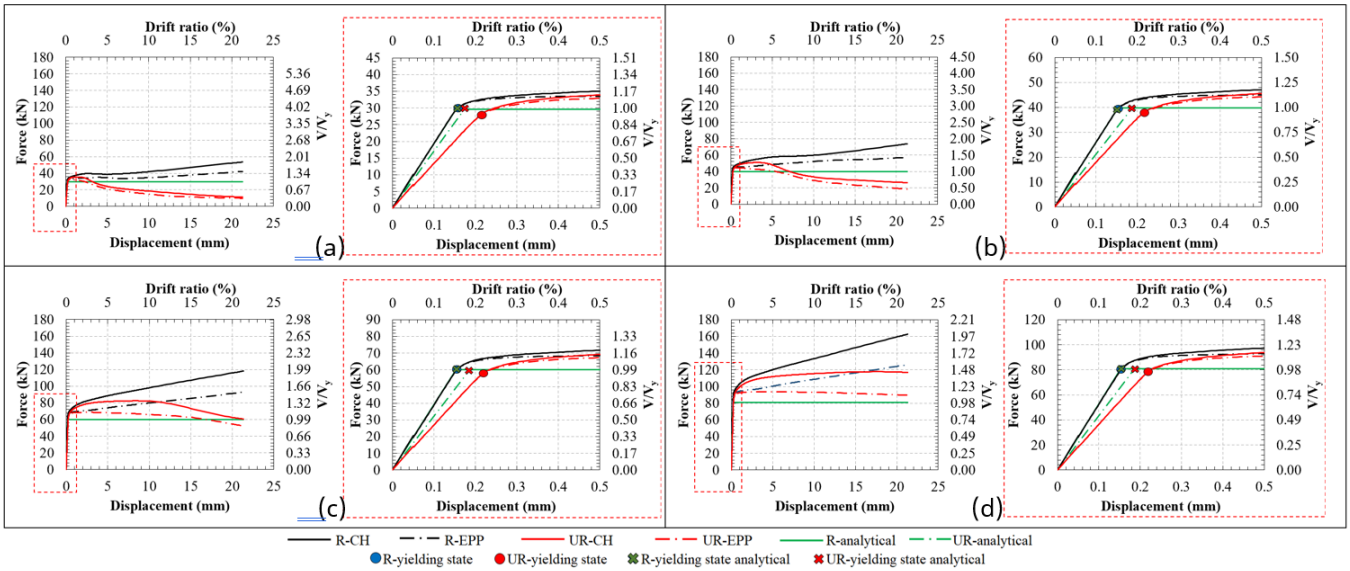

Figure 5 Skeleton curves of BSPD-SHS specimen models with web slenderness (λ); a) 66.7, b) 50.0, c) 33.3, and d) 25.0.

3.2 Shear Strength

Based on the FEA (Table 3 and Fig. 5), the shear yield strength of the restrained model was slightly larger than the unrestrained type. Meanwhile, these results were found to be coincidental in the comparative analytical approach. In the restrained scheme, the replete shear yield stress was also distributed throughout the web depth, as shown in Fig. 5 (a) and (b). However, the unrestrained models emerged with approximately 3% weaker shear yield strength than the analytical approach. This indicated that the UR yield stress distribution along the web depth achieved a more flimsy result, as shown in Fig. 6 (c) and (d).

These results were consistent with the variation of the web slenderness, as the hardening material model did not affect a notable shear yield strength magnitude.

3.3 Post-yield Behaviour

According to the skeleton curve (Fig. 5), all restrained specimens had a stable positive post-yield stiffness, until maximum deformation was achieved in using both CH and EPP models. However, the specimens, SPD-1.5-R-CH, SPD-1.5-R-EPP, SPD-2.0-R-CH, and SPD-2.0-R-EPP, experienced a declined post-yield stiffness and a slight strength reduction. A stable positive post-yield stiffness subsequently reformed till the maximum displacement, indicating that the initial inelastic web buckling occurrence of the models reduced slight strength, with an increase in the stiffening of the web tension-field effect. The comparison of the deformed shape in the maximum displacement is shown in Fig. 7, where the SPD-1.5-R-CH, SPD-1.5-R-EPP, SPD-2.0-R-CH, and SPD-2.0-R-EPP (λ = 66.7 and 50.0) were more significant in buckle occurrence than the slight rele-

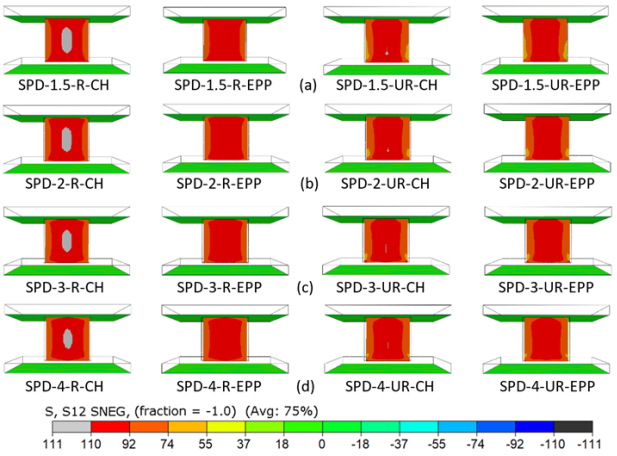

Figure 6 Shear yield stress of the specimen models with web slenderness (λ); a) 66.7, b) 50.0, c) 33.3, and d) 25.0.

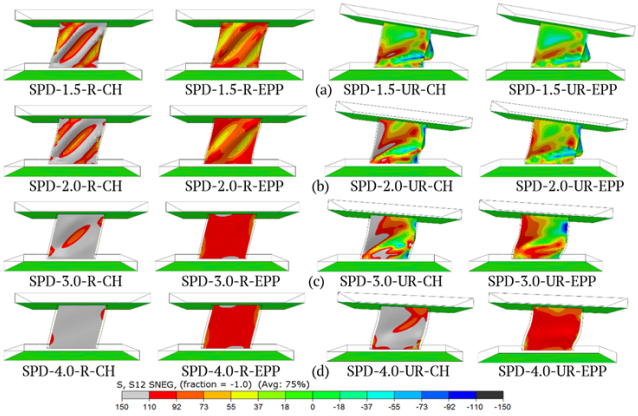

Figure 7 Shear resistance of specimen models in maximum displacement with web slenderness (λ); a) 66.7, b) 50.0, c) 33.3, and d) 25.0.

Table 4. The monitoring of shear yield strength and post-yield shear resistance of the BSPD-SHS

Specimens model	Skeleton curve monitoring			Stress integration		Relative difference		Specimens model	Skeleton curve monitoring			Stress integration		Relative difference	
	$V_{y,sc}$ (kN)	$V_{u,sc}$ (kN)	$V_{u,sc}$ / $V_{y,sc}$	$V_{y,si}$ (kN)	$V_{u,si}$ (kN)	V_y (%)	V_u (%)		$V_{y,sc}$ (kN)	$V_{u,sc}$ (kN)	$V_{u,sc}$ / $V_{y,sc}$	$V_{y,si}$ (kN)	$V_{u,si}$ (kN)	V_y (%)	V_u (%)
SPD-1.5-R-CH	29.86	53.62	1.62	29.89	52.59	0.10	1.92	SPD-3.0-R-CH	60.36	117.03	1.73	60.50	116.81	0.23	0.18
SPD-1.5-R-EPP	29.84	42.11	1.28	29.86	42.36	0.08	0.60	SPD-3.0-R-EPP	60.32	92.69	1.38	60.47	93.50	0.24	0.87
SPD-1.5-UR-CH	28.74	11.95	0.42	28.73	11.86	0.02	0.76	SPD-3.0-UR-CH	58.65	59.67	1.03	58.70	59.48	0.09	0.32
SPD-1.5-UR-EPP	28.62	9.89	0.35	28.61	10.04	0.05	1.60	SPD-3.0-UR-EPP	58.54	50.99	0.88	58.59	51.30	0.08	0.62
SPD-2.0-R-CH	39.94	73.79	1.66	40.00	72.94	0.15	1.15	SPD-4.0-R-CH	81.23	162.75	1.78	81.47	163.46	0.29	0.44
SPD-2.0-R-EPP	39.91	56.77	1.29	39.97	57.77	0.16	1.76	SPD-4.0-R-EPP	81.19	126.16	1.39	81.39	126.54	0.25	0.30
SPD-2.0-UR-CH	38.57	26.10	0.68	38.58	26.38	0.03	1.05	SPD-4.0-UR-CH	79.22	115.56	1.48	79.33	115.21	0.13	0.30
SPD-2.0-UR-EPP	38.44	17.78	0.46	38.43	17.91	0.02	0.74	SPD-4.0-UR-EPP	79.12	89.39	1.14	79.24	88.96	0.15	0.48

vance of the SPD-3.0-R-CH and SPD-3.0-R-EPP (λ = 33.3). Meanwhile, SPD-4.0-R-CH and SPD-4.0-R-EPP (λ = 25.0) are firmly unbuckled under the maximum displacement state. The smaller web slenderness (the thicker web than λ = 25.0) also attained sharper positive post-yield stiffness and was in line with Chan et al. (2009). This indicated that inelastic buckling occurred when the web slenderness was larger than 38.9, accompanied by the slight pinching hysteresis loop. Based on Xu et al. (2016), the stable web was also generated when the slenderness was between 20-25. Although the shear resistance of the maximum displacement specimens was monitored in this study, the seismic device's ductility was still not quantified. This was because the fracture failure model calibrated with the experimental study had not been conducted.

According to Table 4 and Fig. 7, the shear resistance in the maximum displacement increased with the overstrength achievements of 162-178% and 128-139% from the yield stress (V_y), using the CH and EPP models, respectively. These results were in line with Chan et al. (2009), which indicated that all specimens achieved the overstrength factors greater than 1. Based on McDaniel et al. (2003), the overstrength factor was also achieved at approximately 1.83 and 1.94, due to the contribution of the flanges. Meanwhile, the overstrength criteria for the link damper from the AISC/ANSI 341-16 (AISC, 2016a) were determined as 1.25. This indicated that all the specimens achieved stable post-yield stiffness in the restrained top base plate treatment, under the monotonic loading with a 22% drift. Using the CH material, larger shear resistance of 127% was also generated, compared to the utilization of the EPP model.

Based on the unrestrained schemes, a positive-negative phase of post-yield stiffness was observed in the utilization of the CH and EPP materials. In the skeleton curve comparison (Fig. 5 a–d), smaller web slenderness (the thicker web) generated a longer increase-decrease phase. This was in line with the occurrence of significant web and flange buckling as a liability, accompanied by the rotation of the top base plate in SPD-1.5-UR-CH, SPD-1.5-UR-EPP, SPD-2.0-UR-CH, SPD-2.0-UR-EPP, SPD-3.0-UR-EPP, and SPD-3.0-UR-CH (Fig. 7). Based on Table 4 and Fig. 5 (a)–(c), the shear resistance in the maximum displacement decreased between 35-88% of the RSR (residual shear resistance), relative to the yield stress (V_y). Better achievements subsequently showed that SPD-4.0-UR-EPP and SPD-4.0-UR-CH achieved a flat and slightly positive post-yield stiffness with sufficient plastic deformation, respectively, as shown in Fig. 5 (d). Also, the shear resistance of these specimens at the maximum displacement were 114 and 148% relative to the yield stress with buckled slight webs, respectively. Therefore, the BSPD-SHS with a slenderness of 25 was implemented with sufficient post-yield stability in the unrestrained top base plate treatment, under the monotonic loading of 22% drift.

3.4 Shear Stress Integration

According to shear resistance, each stress component on the selected cutting plane, i.e., shear (τ), vertical (σ_y), and horizontal (σ_x) stresses, were integrated and summed based on the theoretical analysis of the thin wall structure (Sabouri-Ghomi et al., 2005). This focused on investigating the stress proportion contribution in web and flange parts. For the finite element analysis, each stress was obtained from the discretization following the meshing size. To accommodate the stress integration in each web and flange, the numerical results in each element discretization was adopted with the trapezoidal method. Additionally, the formulation of the shear resistance was considered in this study, under yielding and post-yield states.

3.4.1 Shear Stress Integration for Shear Strength

Based on the yield deformation state of the prevented elastic buckling design, the shear strength of the specimen was generated by the pure stress of the web components (Sabouri-Ghomi et al., 2005), as illustrated in Fig. 8 (a). This indicated that the web strength was formulated with the numerical integration of the discretized shear stress based on Equation (7), where the δ_{xi} = the element width and τ_i = the shear stress in each element with the assumed web. In the numerical integration, the shear stress of the flange was also considered, although the product was still near zero due to the negation of each element. Based on Table 4, the shear strength from the stress integration (V_y,s_i) had a good agreement with the monitored

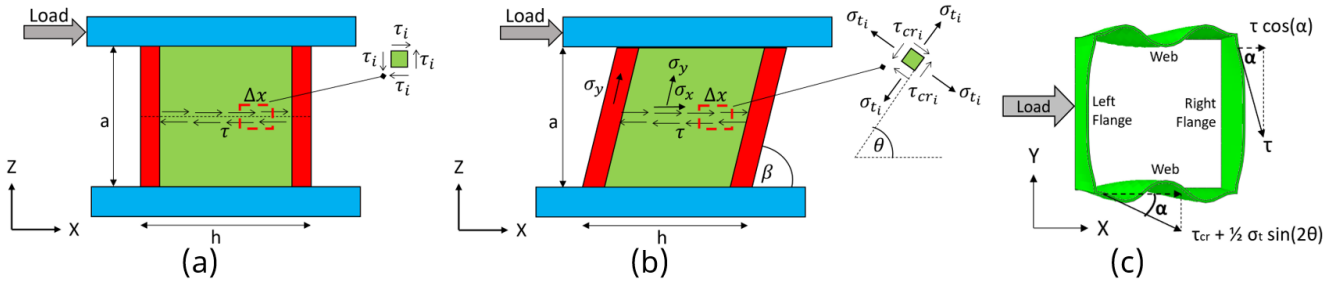

Figure 8 Internal stress action mechanisms in post-yield shear resistance of the BSPD-SHS; (a) pure shear stress (b) with tension-field stress, and (c) shear stress under buckling effect.

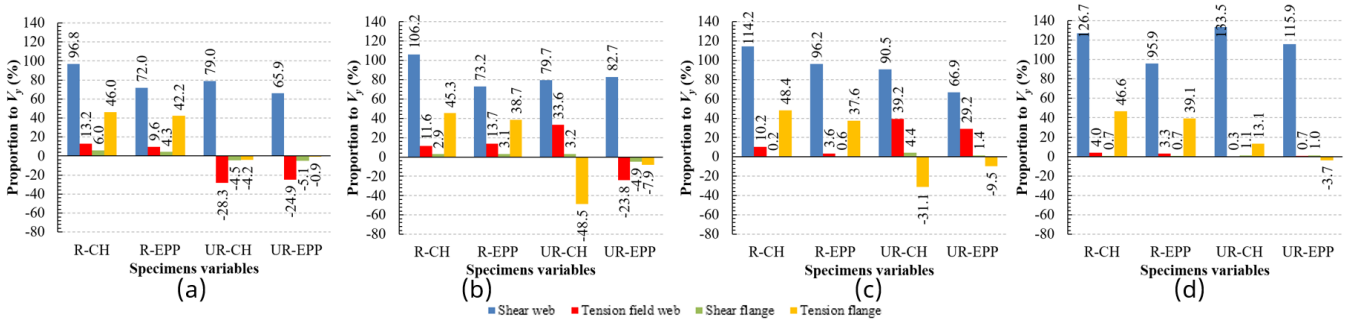

Figure 9 The shear resistance proportion of specimens model under maximum displacement with the variation of restraining and material model when web slenderness (λ) variation; a) 66.7, b) 50.0, c) 33.3, and d) 25.0.

results in the skeleton curve (V_y,s_c).

$$V_y = t_w h\tau = t_w \int_0^h \tau_{(x)} dx = t_w \sum_{i=0}^{h} (\delta x_i \tau_i) \quad (7)$$

3.4.2 Shear Stress Integration for Post-yield Resistance

According to the post-yield deformation, the occurrence of the web or flange buckling was observed, indicating that the tension-field action should be considered (Sabouri-Ghomi et al., 2005). This showed that the web shear resistance was formulated with the numerical integration of critical and tension-field stresses with the length of the element discretization. These results were based on Equation (8), where τ_{cr}, i and σ_t, i = the maximum critical shear and tension-field stresses, with θ_i and γ_i is being the oriental angle and rotation surface in the vertical axis, respectively. Moreover, the notation of "i" subscript indicated the element identity. In this analysis, the $\tau_c r, i$, σ_t, i, and θ_i were determined in the maximum shear stress state regarding Equation (9) (Dowling, 2013). The flanges also contributed to the production of resistance with tension-field and shear stress action of the components, based on the buckled state. When the seismic device significantly deformed in the lateral direction inclined with an angle of β, the flanges normal stress (σ_y) was formed, as shown in Fig. 8 (b). With the inclined angle (β) and normal stress (σ_y) multiplied by the flange area, the lateral resistant force was produced, due to the tension field of the material. Also, the flange surface inclined with an angle of γ_i provoked the shear stress when buckling occurred, as shown in Fig. 8 (c). The lateral resistant force was also generated by the flange shear stress (τ_i), multiplied by the area and the inclined angle of the material. This indicated that the contribution of the resisting lateral force was produced by the tension-field and shear stress actions of the flange, as shown in Equation (10).

$$\begin{aligned} V_{u,w} &= t_w h \left(\tau_{cr(x)} + \frac{1}{2}\sigma_{t(x)} sin2\theta_{(x)} \right) cos\alpha_{(x)} \\ &= t_w \int_0^h \left[\left(\tau_{cr_{(x)}} + \frac{1}{2}\sigma_{t(x)} sin2\theta_{(x)} \right) cos\alpha_{(x)} \right] dx \\ &= t_w \sum_{i=0}^{h} \left[\left(\tau_{cr,i} + \frac{1}{2}\sigma_{t,i} sin2\theta_i \right) cos\alpha_i \delta x_i \right], \end{aligned} \quad (8)$$

$$\text{With} \quad \tau_{cr} = \sqrt{\left(\frac{\sigma_x - \sigma_y}{2}\right)^2 + \tau^2}; \quad \sigma_t = \frac{\sigma_x + \sigma_y}{2};$$
$$\text{and} \quad \theta = \frac{1}{2} arctan\left(-\frac{\sigma_x - \sigma_y}{2\tau}\right) \tag{9}$$

$$= t_w \sum_{i=0}^{h} \left[\left(\sigma_{y,i} cos\beta + \tau_i cos\alpha_i\right) \delta x_i\right]. \tag{10}$$

$$V_u = 2V_{u,w} + V_{u,fr} + V_{u,fl} \tag{11}$$

Based on this study, the total BSPD-SHS post-yield shear resistance (V_u) was obtained by summing the lateral resistant force of the webs and flanges, as formulated in Equation (11). Where, $V_{u,\,w}$, $V_{u,\,fr}$, and $V_{u,\,fl}$ = the web, as well as the right and left flanges shear resistances, respectively. Based on Table 4, the post-yield shear resistance from the proposed stress integration ($V_{u,\,si}$) was in line with the monitored results obtained from the skeletal curve ($V_{u,\,sc}$).

When the shear and tension-field resistances of the web and flange were distinguished and compared with the strength, the obtained contributions were illustrated in Fig. 9. Using restrained (R) top base plate with the CH model (R-CH), the contributions of the WSR (web shear resistance) increased with the smaller slenderness between 96.8-126.7%, while the WTF (web tension-field) and FSR (flange shear resistance) decreased between 13.2-4.0% and 6.0-0.7%, respectively. Meanwhile, the contribution of the flange tension field was almost constant at approximately 46%. Using the restrained (R) top base plate with the EPP model (R-EPP), the shear resistance contribution trend increased between 72.0-96.2%. At λ = 50.0, the contribution of the web shear resistance was also 95.9%. However, the contributions of the web tension-field and flange shear resistance were slightly weaker than the R-CH condition, except in the case of λ = 50.0. The contribution of the tension-field flanges was also found to be almost constant at approximately 39.0%. Meanwhile, the study of Chen et al. (2006)indicated that the common SPD flanges increased post-yield resistance between 13-20%, towards the total ultimate strength. The square hollow section configuration also highly increased the stable flange, compared to the common SPD, due to the web confinement in its edges.

Using restrained (UR) top base plate with the CH model (UR-CH), the contributions of the WSR (web shear resistance), WTF (web tension-field), and FSR (flange shear resistance) patterns increased with smaller slenderness between 79.0-133.5%, -28.3-39.2%, and -4.5-4.4%, respectively. Meanwhile, the contribution of the tension-field flange was uncertain between -48.4%-13.1%. Using an unrestrained (UR) top base plate with the EPP model (UR-EPP), the web shear resistance contribution increased between 65.9-115.0%, although dropped to 66.9% when λ = 33.3. The contributions of the web tension field and the flange shear resistance were also slightly weaker than the UR-CH case. However, the tension-field flange contribution was almost zero, with the most significant being -9.5%. This indicated that several negative contributions were observed in the WTF, FSR, and FTF (flange tension-field). Therefore, improvements were not observed in the shear resistance contribution, due to the high rate of reduction.

4 CONCLUSIONS AND RECOMMENDATIONS

Based on the finite element analysis of the BSPD-SHS model in this preliminary study, the elastic stiffness, shear strength, post-yield behavior, stress actions with variable slenderness, restraining schemes, and material models were investigated. This study indicated that the elastic stiffness of the restrained schemes achieved coincidental results than the analytical approach. However, more flexible stiffness of the unrestrained schemes still specifically need to be studied. For the shear strength, the finite element analysis was adequately estimated, as the restraint (R) of the top base plate treatment produced stable post-yield shear resistance with positive stiffness. Using the unrestrained (UR) top base plate, a stable post-yield shear resistance was only produced when the slenderness was 25.0. In addition, the combined hardening model generated larger post-yield shear resistance with sharper stiffness, compared to the utilization of the elastic-perfectly plastic material. The contributions of the web and flange resistances were also investigated in this study. This indicated adequate coincidental results with the analytical stress action formulation of the components in each shear and tension field, based on yielding and post-yield deformation. Using the restrained (R) top base plate, the shear

stress of the webs and tension field of the flanges dominantly contributed to the post-yield resistance at approximately 72-126% and 37.6-48.4%, respectively. Meanwhile, the variated composition of the stress component contributions dominantly occurred with the web shear resistance when using the unrestrained (UR) schemes of the top flange. Besides these results, several tension-field of the webs and flanges detracted the shear resistance. When the slenderness was found at 25.0, almost only the web shear stress generated resistance. Based on the stable post-yield behavior achievement, the implementation of a restrained (R) top base plate of BSPD-SHS is highly recommended when the slenderness (λ) is between 66.7-25.0. This plate should also be treated with unrestrained (UR) schemes when the maximum slenderness (λ) is $\leqslant$ 25.0. Based on these results and recommendations, further future studies should be conducted on the shear resistance behavior and variated load angles of the BSPD-SHS. Also, further reports should be conducted on the BSPD-SHS shear resistance behavior under cyclic loading, to investigate the seismic performance.

DISCLAIMER

The authors declare no conflict of interest.

AVAILABILITY OF DATA AND MATERIALS

All data are available from the author.

ACKNOWLEDGMENTS

The authors are grateful to the Material Laboratory, Structural Laboratory, and Head of the Department in Civil and Environmental Engineering Department, Faculty of Engineering, Universitas Gadjah Mada, for supporting this study. The authors are also grateful to the Indonesian Research and Technology Ministry and PT Wijaya Karya Beton Tbk, for financially supporting this study through the SIMLITABMAS program.

REFERENCES

Abebe, D. Y., Kim, J. W., Gwak, G. and Choi, J. H. (2019), 'Low-cycled hysteresis characteristics of circular hollow steel damper subjected to inelastic behavior', *International Journal of Steel Structures* **19**(1), 157–167.

AISC (2016a), 'Seismic provisions for structural steel buildings', *Chicago, Illinois, USA: American Institute of Steel Construction (AISC)* pp. 341–16.

AISC (2016b), 'Seismic provisions for structural steel buildings', *Chicago, Illinois, USA: American Institute of Steel Construction (AISC)* pp. 360–16.

Chaboche, J.-L. (1986), 'Time-independent constitutive theories for cyclic plasticity', *International Journal of plasticity* **2**(2), 149–188.

Chan, R. W., Albermani, F. and Williams, M. S. (2009), 'Evaluation of yielding shear panel device for passive energy dissipation', *Journal of Constructional Steel Research* **65**(2), 260–268.

Chaofeng, Z., Youchun, W., Longfei, W. and Meiping, W. (2017), 'Hysteretic mechanical property of low-yield strength shear panel dampers in ultra-large plastic strain', *Engineering Structures* **148**, 11–22.

Chen, Z., Ge, H. and Usami, T. (2006), 'Hysteretic model of stiffened shear panel dampers', *Journal of structural engineering* **132**(3), 478–483.

Chen, Z., Ge, H. and Usami, T. (2007), 'Study on seismic performance upgrading for steel bridge structures by introducing energy-dissipation members', *Journal of Structural Engineering, A* **53**, 540–549.

Dassault-Systèmes, A. (2011), 'Standard analysis user's manual', *Dassault Systèmes Simulia Corp., Providence, RI, USA* .

Dowling, N. E. (2013), *Mechanical Behavior of Materials. 4th ed. Harlow: Pearson Education*, Pearson Education.

Effendi, M. K. (2020), Non-linear finite element analysis of flexural reinforced concrete beam using embedded reinforcement modeling, *in* 'Journal of the Civil Engineering Forum', Vol. 6, pp. 271–284.

Ge, H., Chen, X. and Kang, L. (2012), 'Demand on stiffened steel shear panel dampers in a rigid-framed bridge pier under repeated seismic ground motions', *Advances in Structural Engineering* **15**(3), 525–546.

Hashimoto, K., Otsuka, K., Sugiura, K., Sugiyama, Y. and Kanaji, H. (2016), 'Effect of structural parameters of shear panel damper on seismic performance of multi-pipe integrated bridge pier', *Journal of Japan Society of Civil Engineers, Ser. A1 (Structural Engineering & Earthquake Engineering (SE/EE))* **72**(1), 75–91.

Jin, K., Guo, X., Tao, J., Wang, H., Kim, N. and Gu, Y. (2016), 'A model of one-surface cyclic plasticity with lemaitre damage criterion for plastic instability prediction in the incremental forming process', *International Journal of Mechanical Sciences* **114**, 88–97.

Maleki, S. and Bagheri, S. (2010), 'Pipe damper, part i: Experimental and analytical study', *Journal of Constructional Steel Research* **66**(8-9), 1088–1095.

McDaniel, C. C., Uang, C.-M. and Seible, F. (2003), 'Cyclic testing of built-up steel shear links for the new bay bridge', *Journal of Structural Engineering* **129**(6), 801–809.

NAKAMURA, R., KANAJI, H. and KOSAKA, T. (2014), Development and design of new steel pipe integrated pier with shear link, Technical report, Technical report, Hanshin Expressway Company Limited, Osaka.

Narendra, P. V., Prasad, K., Krishna, E. H., Kumar, V. and Singh, K. D. (2019), Low-cycle-fatigue (lcf) behavior and cyclic plasticity modeling of e250a mild steel, *in* 'Structures', Vol. 20, Elsevier, pp. 594–606.

Nuzzo, I., Losanno, D., Caterino, N., Serino, G. and Rotondo, L. M. B. (2018), 'Experimental and analytical characterization of steel shear links for seismic energy dissipation', *Engineering Structures* **172**, 405–418.

Sabouri-Ghomi, S., Ventura, C. E. and Kharrazi, M. H. (2005), 'Shear analysis and design of ductile steel plate walls', *Journal of Structural Engineering* **131**(6), 878–889.

Shi, G., Gao, Y., Wang, X. and Zhang, Y. (2018), 'Mechanical properties and constitutive models of low yield point steels', *Construction and Building Materials* **175**, 570–587.

Shirinkam, M. R. and Razzaghi, J. (2020), Experimental and analytical investigation on the behavior of metallic box-shaped dampers (bsd), *in* 'Structures', Vol. 23, Elsevier, pp. 766–778.

Sun, J., Manzanarez, R. and Nader, M. (2004), 'Suspension cable design of the new san francisco–oakland bay bridge', *Journal of Bridge Engineering* **9**(1), 101–106.

Tetsuhiko, A. (2011), 'Shear-panel type damper, bearing structure of bridge using the same, and the bridge adopting the bearing structure.'.

Tetsuhiko, A., F., Y. and Tatsumasa (2010), 'Shear panel-type damper and bridge.'.

Vasseghi, A. (2011), 'Energy dissipating shear key for precast concrete girder bridges', *Scientia Iranica* **18**(3), 296–303.

Xu, L.-Y., Nie, X. and Fan, J.-S. (2016), 'Cyclic behaviour of low-yield-point steel shear panel dampers', *Engineering Structures* **126**, 391–404.

Xu, W., Wang, S., Liu, W. and Du, D. (2020), 'Experimental study on mechanical properties of shear-type mild steel damper', *International Journal of Structural and Civil Engineering Research* **9(1)**, 57–63.

Yamaguchi, T., Nakata, Y., Takeuchi, T., Ikebe, T., Nagao, T., Minami, A. and Suzuki, T. (1998), 'Seismic control devices using low-yield-point steel; gokuteikofukutenko, teikofukutenko wo riyoshita seishin gijutsu no kaihatsu', *Shinnittetsu Giho* **368**, 61–67.

Yasuhisa, H., Satoji, O., Masaru, S., Kazunari, T., Sadafumi, U. and Akihisa, Y. (2007), 'Shear pane form seismic response control blade latch.'.